

## Influence of relative humidity on aerosol radiative forcing: An ACE-Asia experiment perspective

Krzysztof M. Markowicz,<sup>1</sup> Piotr J. Flatau,<sup>2,3</sup> P. K. Quinn,<sup>4,5</sup> Christian M. Carrico,<sup>6,7</sup>  
M. K. Flatau,<sup>2</sup> A. M. Vogelmann,<sup>3</sup> David Bates,<sup>8</sup> M. Liu,<sup>2</sup> and Mark J. Rood<sup>7</sup>

Received 22 October 2002; revised 16 January 2003; accepted 3 March 2003; published 27 August 2003.

[1] We present direct radiometric observations of aerosol radiative forcing during the ACE-Asia experiment (March and April of 2001). The observational analysis is based on radiometer data obtained from the NOAA ship *Ronald H. Brown*, and shipboard measurements of the aerosol chemical and scattering properties are used to construct a model of the aerosol optical properties for use in radiative transfer calculations. The model is validated against the radiometric observations and is used to diagnose the aerosol and environmental factors that contribute to the observed forcings. The mean value of aerosol optical thickness observed during the ACE-Asia cruise over the Sea of Japan was 0.43 ( $\pm 0.25$ ) at 500 nm, while the single-scattering albedo was 0.95 ( $\pm 0.03$ ) at ambient relative humidity. We find a large correlation ( $r^2 = 0.69$ ) between single-scattering albedo and relative humidity. Aerosols caused a mean decrease in the diurnally averaged solar radiation of  $26.1 \text{ W m}^{-2}$  at the surface, while increasing the atmospheric solar absorption and top of atmosphere reflected solar radiation by  $13.4 \text{ W m}^{-2}$  and  $12.7 \text{ W m}^{-2}$ , respectively. The mean surface aerosol forcing efficiency (forcing per unit optical depth) over the Sea of Japan was  $-60 \text{ W m}^{-2}$  and is influenced by high values of relative humidity. We show that decreasing the relative humidity to 55% enhances the aerosol forcing efficiency by as much as  $6-10 \text{ W m}^{-2}$ . This dependency on relative humidity has implications for comparisons of aerosol forcing efficiencies between different geographical locations. **INDEX TERMS:** 0305 Atmospheric Composition and Structure: Aerosols and particles (0345, 4801); 0345 Atmospheric Composition and Structure: Pollution—urban and regional (0305); 1640 Global Change: Remote sensing; 3307 Meteorology and Atmospheric Dynamics: Boundary layer processes; 3359 Meteorology and Atmospheric Dynamics: Radiative processes; **KEYWORDS:** aerosol, forcing, ACE-Asia, humidity, optical depth

**Citation:** Markowicz, K. M., P. J. Flatau, P. K. Quinn, C. M. Carrico, M. K. Flatau, A. M. Vogelmann, D. Bates, M. Liu, and M. J. Rood, Influence of relative humidity on aerosol radiative forcing: An ACE-Asia experiment perspective, *J. Geophys. Res.*, 108(D23), 8662, doi:10.1029/2002JD003066, 2003.

### 1. Introduction

[2] The effects of sea salt, mineral dust, black carbon, and sulfates in complex environmental conditions are one of the largest sources of uncertainty in quantifying regional climate changes [*Intergovernmental Panel on Climate*

*Change*, 2001]. Much recent work has been devoted to reducing these uncertainties using global circulation models [*Chin et al.*, 2002; *Takemura et al.*, 2002], transport models [*Collins et al.*, 2001], observational networks [*Holben et al.*, 2001], satellite observations [*Wielicki*, 1996], and by mounting major observational campaigns (SCAR-B [*Kaufman et al.*, 1998], TARFOX [*Hobbs*, 1999], ACE1 [*Bates et al.*, 1998], ACE2 [*Raes et al.*, 2000], INDOEX [*Ramanathan et al.*, 2001], MINOS [*Lelieveld et al.*, 2002]). Progress has been reported thanks to these complementary activities.

[3] Determining the radiative effects of very small particles in the atmosphere requires observations of aerosol chemistry, knowledge of the aerosol optical properties, and precise radiometric measurements at the surface and top of atmosphere. Recent international studies such as Indian Ocean Experiment (INDOEX) and Mediterranean Intensive Oxidants Study (MINOS) revealed much about the radiative properties of regional aerosols, but were purposefully set in meteorologically simple environments. INDOEX was under the influence of steady pre-monsoonal winds, and MINOS was in the steady summer trades of the Central and Eastern

<sup>1</sup>Institute of Geophysics, University of Warsaw, Warsaw, Poland.

<sup>2</sup>Naval Research Laboratory, Monterey, California, USA.

<sup>3</sup>Center for Atmospheric Sciences, Scripps Institution of Oceanography, University of California, San Diego, La Jolla, California, USA.

<sup>4</sup>Pacific Marine Environmental Laboratory, NOAA, Seattle, Washington, USA.

<sup>5</sup>Joint Institute for the Study of the Atmosphere and Ocean, University of Washington, Seattle, Washington, USA.

<sup>6</sup>Department of Atmospheric Science, Colorado State University, Ft. Collins, Colorado, USA.

<sup>7</sup>Department of Civil and Environmental Engineering, University of Illinois at Urbana-Champaign, Urbana, Illinois, USA.

<sup>8</sup>Physics Department, University of Miami, Coral Gables, Florida, USA.

Mediterranean [Lelieveld *et al.*, 2002]. In contrast, this study determines the radiative effects of aerosols during the Asian Pacific Regional Aerosol Characterization Experiment (ACE-Asia), which took place in the spring of 2001 and was designed to study the complex outflow of mineral dust and air pollution from Asia at mid-latitudes. Our instruments were located on NOAA ship *Ronald H. Brown*, and we sailed from Honolulu, Hawaii to the Sea of Japan. On the Pacific transect we were able to observe passages of extratropical cyclones and long-range pollution transport. The sampling near the Asian coast found both pollution and dust from the arid regions of Asia. During part of the cruise, we crossed the oceanic polar front at 38°N in the Sea of Japan, which largely determined the sea surface temperature and relative humidity. We observed hazy conditions when the water was cool and the relative humidity was high.

[4] The role of relative humidity on aerosol radiative properties has been investigated in transport models by assuming humidity growth factors for various aerosols [Chin *et al.*, 2002; Takemura *et al.*, 2002] and the role of hygroscopic growth on direct radiative forcing at the surface was shown recently to be significant [Im *et al.*, 2001; Kotchenruther *et al.*, 1999]. In retrospect, the meteorological setting of several recent field projects was such that large relative humidity gradients were observed between either between the land and ocean, or between the regions of descending and ascending branches of Hadley circulation. We will show that these conditions are important when estimating aerosol radiative effects in terms of the aerosol forcing efficiency, which has become a common means for quantifying aerosol radiative effects on the Earth's energy balance. (Aerosol forcing is defined as the radiative flux when aerosols are present minus when they are absent, and the aerosol forcing efficiency is the aerosol forcing per unit optical depth [Satheesh and Ramanathan, 2000].)

[5] In this paper, we determine directly from radiometric observations the aerosol radiative forcing at the surface and top of atmosphere. Shipboard measurements of the aerosol chemical and scattering properties are used to construct a model of the aerosol optical properties for use in radiative transfer calculations. The model is validated against the radiometric observations, and is used to diagnose the aerosol and environmental factors that contribute to the observed forcings. This analysis reveals the importance of relative humidity to the aerosol forcing efficiency.

[6] The paper is organized as follows. Section 2 describes the radiometric and aerosol chemical and scattering measurements that were used. The radiometric observations include the surface observations of the aerosol optical depth and broadband fluxes, and the top of atmosphere satellite fluxes. We also describe the surface measurements of aerosol chemistry and scattering properties, and the lidar measurements of the aerosol extinction within the column. These measurements are used to construct the aerosol optical model described in section 3, which is used in a radiative transfer model to assist with the data interpretation. Section 4 discusses the observations of aerosol optical thickness, and validates the aerosol model via a comparison of the computed and observed single-scattering albedos. This provides the background for section 5 that determines

aerosol forcing directly from the radiometric observations, and these observations are used to validate the model calculations. Section 6 examines the influence of relative humidity on aerosol forcing efficiency, and section 7 contains the summary and discussion.

## 2. Instrumentation

[7] This section describes the radiometric data that are used in the observational determination of the aerosol forcing efficiency. We also describe the observations of the aerosol vertical distribution, size distribution, composition, and scattering and absorption coefficients that are used to construct the aerosol optical model in section 3.

[8] During the ACE-Asia field project we performed radiation measurements on board the NOAA research ship *Ronald H. Brown* (Figure 1). Total broadband (280–2800 nm) radiative fluxes were obtained using CM21 Kipp and Zonen pyranometers. According to the technical specification provided by the manufacturer, this instrument has an absolute accuracy of  $\pm 9 \text{ W m}^{-2}$  and the maximum flux error due to a simplified cosine response is  $\pm 10 \text{ W m}^{-2}$ . To minimize the ship's pitch and roll, we mounted the pyranometers on gimbaled (moving) suspension.

[9] Two handheld Microtops II (Sun photometer and Ozonometer) [Morys *et al.*, 2001] with spectral filters for visible and near-infrared (NIR) wavelengths were used to retrieve aerosol optical thickness (AOT), columnar water vapor, and columnar ozone. The AOT was measured at 380, 440, 500, 675, 870 nm by the Sun photometer and at 1020 nm by the Ozonometer. The total water column was obtained from the Sun radiance measured at 936 and 1020 nm. The Microtops were calibrated at the Mauna Loa Observatory, Hawaii, just after the field phase of ACE-Asia, and we post-processed the data using the new calibration constants. The absolute accuracy of these instruments is about 2% but the error in the derived total optical thickness is largest for low solar zenith angles. Therefore the accuracy of the AOT is about 0.01 at 500 nm. The Microtops is a handheld instrument that has a convenient, albeit time consuming, procedure to minimize the pitch and roll errors. To minimize the pitch and roll effect, each Microtops observation includes 5 independent scans. The scan with largest signal was used, which corresponds to the best instrument-Sun alignment.

[10] Vertical profiles of the aerosol extinction coefficient at 523 nm were measured by a micropulse lidar (MPL) [Welton *et al.*, 2000]. The vertical resolution of this instrument is 75m. The aerosol extinction coefficient was obtained from the calibrated lidar signal and the Microtops observations of the AOT. In this study the backscatter-to-extinction ratio (BER) is treated as constant with respect to distance through an aerosol layer. However, the BER ratio of each individual layer can change depending upon the phase function and single-scattering albedo. For example, during the ACE-Asia this parameter varied between 25 and 118. Fortunately, the solar radiative forcing discussed here is not overly sensitive to the choice of extinction profiles.

[11] Concentrations of chemical components in the sub- and supermicron size ranges were determined by NOAA's Pacific Marine Environmental Laboratory (PMEL). The analyzed components include sea salt, sulfate, nitrate, total

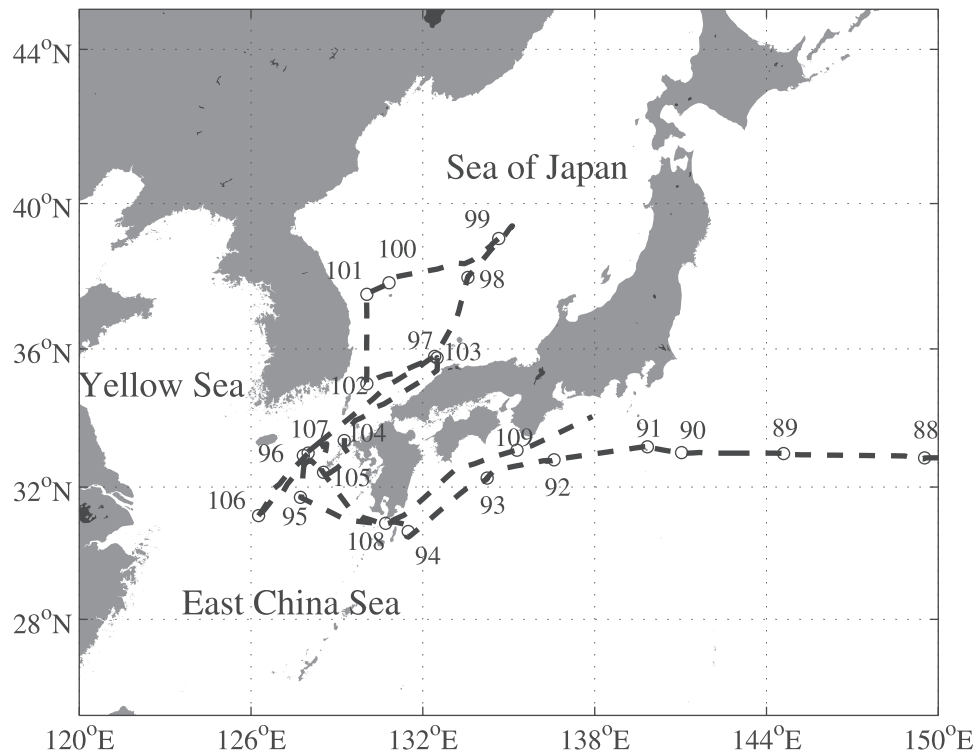


**Figure 1.** NOAA ship *Ronald H Brown* track during the ACE-Asia cruise between Honolulu and Yokosuka in March and April 2001.

organic carbon, elemental carbon, and dust. Submicron and supermicron refer to all particles with aerodynamic diameters less than  $1\ \mu\text{m}$  and between  $1$  and  $10\ \mu\text{m}$ , respectively, at 55% relative humidity (RH). The last 1.5 m of the mast was heated to establish a stable reference RH for the sample air of  $55 \pm 5\%$ . A stable reference RH allows for constant instrumental size segregation in spite of variations in ambient RH, and results in chemical, physical, and optical measurements that are directly comparable. In addition, measurement at a constant reference RH makes it possible, with the knowledge of appropriate growth factors, for end users of the data set (process, chemical transport, and radiative transfer models) to adjust the measured parameters to a desired relative humidity. A reference RH 55% was chosen because it has been shown to reduce impactor bounce, since there is enough water associated with the hygroscopic aerosol species at this RH to make the aerosol “sticky”. In addition, for the atmospheric conditions encountered during Ace Asia, it was possible to maintain 55% RH without excessive heating of the aerosol.

[12] The methodology of the chemical analysis is described elsewhere [cf. Quinn *et al.*, 2001, 2002]. We divided the chemical species into several groups according to their physical properties: sulfate and nitrate aerosol mass, sea-salt mass, total organic carbon, elemental carbon, and dust. The concentration of dust was derived assuming that all elements were in their common oxide form [Malm *et al.*, 1994]. The particulate organic matter (POM) was determined from the measured organic carbon concentration and the expression  $\text{POM} = 2.1 \times \text{OC}$  ( $\mu\text{g m}^{-3}$ ) [Turpin and Lim, 2001]. On the basis of these mass concentrations, we associated the optical properties with these chemical components.

[13] The aerosol absorption coefficient at the surface was obtained from the Particle Soot Absorption Photometer (PSAP) produced by Radiance Research [Bond *et al.*, 1999]. Measured values were corrected for a scattering artifact, the deposit spot size, the PSAP flow rate, and the manufacturer’s calibration. Values are reported at 550 nm. Sources of uncertainty in the PSAP measurement include noise, drift, correction for the manufacturer’s calibration, and correction for the scattering artifact [Bond *et al.*, 1999]. A quadrature sum of these errors yields absolute uncertainties of 0.38 and 0.68 for an absorption coefficient equal to  $2.8 \times 10^{-6}\ \text{m}^{-1}$  and  $13 \times 10^{-6}\ \text{m}^{-1}$ , respectively, for a 30 minute averaging time. Measurements of aerosol scattering and hemispheric backscattering coefficients were made with an integrating nephelometer (Model 3563, TSI Inc.) at wavelengths of 450, 550, and 700 nm at  $55 \pm 10\%$  RH and sub-10 micron (particles with diameter less than  $10\ \mu\text{m}$ ) data were used. The RH was measured inside the nephelometer sensing volume. Values measured directly by the nephelometer are corrected for an offset determined by measuring filtered air over a period of several hours [Anderson and Ogren, 1998]. In addition, they were corrected for the angular nonidealities, including truncation errors and nonlambertian response of the nephelometer as per Anderson and Ogren [1998].

[14] The PMEL PSAP and nephelometer were kept at  $55 \pm 10\%$  relative humidity. In addition, the aerosol light scattering as a function of relative humidity was measured using controlled relative humidity nephelometry (humidograph) [Carrico *et al.*, 1998]. The aerosol sample was scanned from an RH of 35 to 85% over an hourly cycle time while continually measuring the aerosol light scattering at 450, 550, and 700 nm. To investigate hysteresis effects from

metastable droplet formation, RH scans were performed with increasing RH beginning with a “dry” aerosol and with decreasing RH beginning with a hydrated aerosol [Carrico *et al.*, 2000]. We used data from both increasing and decreasing RH regimes and discuss this point in more detail while presenting results.

[15] The top of atmosphere (TOA) fluxes were obtained from the CERES instrument onboard the TERRA satellite (the resolution of CERES is 20 km at nadir). CERES measures radiances, which are converted to fluxes using angular distribution models [Loeb and Kato, 2002]. In this study we use Beta 2 SSF CERES data. One of the largest sources of uncertainty in estimating the outgoing shortwave fluxes from satellite measurements is cloud contamination. However, in this study, only days without clouds (base on observations from ship) were used. The second source of uncertainty involves the radiance to flux conversion. We used the newer version of the CERES angular model [Loeb and Kato, 2002], which reduced uncertainty of the older (ERBE-like) CERES product.

### 3. Aerosol Model

[16] Although we emphasize observational analyses in this paper, we use an aerosol model and radiative transfer calculations to help with the data interpretation. After its validation, the aerosol model is used to determine properties that we were not able to measure directly. For example, we used the aerosol model to derive the top of the atmosphere forcing for days when CERES data were not available (section 5). Also, because our data set is limited, we use the radiative transfer model results to help interpretate the effects of relative humidity on the aerosol forcing results (section 6).

[17] The aerosol model is constructed from the chemical measurements, combined with tabulated information about the aerosol radiative properties. Specifically, the optical properties such as extinction, absorption coefficient, and asymmetry parameter are obtained as a function of wavelength and relative humidity from the Optical Properties of Aerosol and Clouds software (OPAC 3.1) [Hess *et al.*, 1998]. The OPAC data set describes optical properties for 10 aerosol components: insoluble, water-soluble, soot, sea salt (accumulation and coarse mode), mineral (nucleation, accumulation, coarse mode), mineral (transported), and Antarctic sulfate droplets. The data are available at 61 wavelengths between 0.25 and 40  $\mu\text{m}$ , and for eight RH (0, 50, 70, 80, 90, 95, 98, 99%). Lognormal size distributions define each component. In the OPAC database the assumption is made that particles are spherical and externally mixed, although soot and dust particles can coagulate to form complex clusters. We have performed preliminary study of simple soot-dust configurations using cluster of spheres calculations [Flatau *et al.*, 1993] and noticed only small absorption enhancements.

[18] Out of ten possible OPAC classes, we define only six aerosol types: water-soluble, soot, sea-salt accumulation and coarse modes, and mineral dust accumulation and coarse modes. The “soluble” category includes sulfate (including sea-salt and non-sea-salt sulfate), nitrate, and POM. By assuming that POM is “soluble” we specify that its optical and hygroscopic properties are similar to sulfates [Chin *et*

*al.*, 2002]. The extent of water uptake by the POM measured during ACE Asia is largely unknown, however, and the actual growth may be less than that of sulfates. The “soot” category includes elemental carbon and the mass of “dust” category is defined as  $\text{Mass} = 2.2\text{Al} + 2.49\text{Si} + 1.63\text{Ca} + 2.42\text{Fe} + 1.94\text{Ti}$  which converts the major elements in dust to their common oxide form [Malm *et al.*, 1994].

[19] For the given dry aerosol mass density ( $\mu\text{g m}^{-3}$ ) in each category, we assume a growth factor [Hanel and Zankl, 1979] and calculate the aerosol mass at 55% RH. From these masses we calculate submicron and supermicron number density of particles (number of particles per cubic cm). These are the number densities that are subsequently used by OPAC to define the optical properties.

[20] The aerosol chemical composition is assumed to be constant with altitude, but the vertical optical properties change with height because of humidity changes. This assumption is good for the boundary layer, but may be poor for decoupled upper layers such as dust. Numerical models and lidar did show the presence of layered structures during the cruise. However, our assumption is realistic because typically the aerosol optical depth is concentrated in the boundary layer. The atmospheric soundings of temperature, pressure, and relative humidity were obtained every 3 hours. On the basis of the particles number density, we calculated the normalized extinction at 550 nm, and absorption coefficients from OPAC. These values were scaled by the vertical profile of aerosol extinction at 550 nm, obtained from MPL lidar observations at 523 nm. The small mismatch of observational wavelengths in this case does not influence the results because we use only the normalized extinction profile, not its absolute value.

[21] The optical properties determined in our aerosol model are used in radiative transfer calculations in sections 5 and 6 to determine the radiative fluxes at the surface and top of atmosphere. For these calculations, we need from our aerosol model the vertical distributions of the aerosol extinction coefficient, absorption coefficient, and asymmetry parameter as a function of wavelength. The averages of these scattering properties are determined from our model for two layers (0–2 km, 2–10 km) as

$$\langle \tilde{\sigma}_{ext}(\lambda) \rangle = \frac{\int \sigma_{ext}^{550}(z) \tilde{\sigma}_{ext}(\lambda, RH(z)) dz}{\int \sigma_{ext}^{550}(z) dz} \quad (1)$$

$$\langle \tilde{\sigma}_{abs}(\lambda) \rangle = \frac{\int \sigma_{ext}^{550}(z) \tilde{\sigma}_{abs}(\lambda, RH(z)) dz}{\int \sigma_{ext}^{550}(z) dz} \quad (2)$$

$$\langle g_{ext}(\lambda) \rangle = \frac{\int \sigma_{ext}^{550}(z) g(\lambda, RH(z)) \omega(\lambda, RH(z)) dz}{\int \sigma_{ext}^{550}(z) \omega(\lambda, RH(z)) dz} \quad (3)$$

where  $\sigma_{ext}^{550}(z)$  is the lidar vertical profile of aerosol extinction coefficient scaled by aerosol optical thickness,  $\tilde{\sigma}_{ext}(\lambda, RH(z))$  and  $\tilde{\sigma}_{abs}(\lambda, RH(z))$  are the spectral and relative humidity functions of the extinction and absorption coefficients normalized to extinction at 550 nm,  $\omega(\lambda, RH(z))$  is the single-scattering albedo, and  $g(\lambda, RH(z))$  is the asymmetry parameter. The OPAC database has its strengths

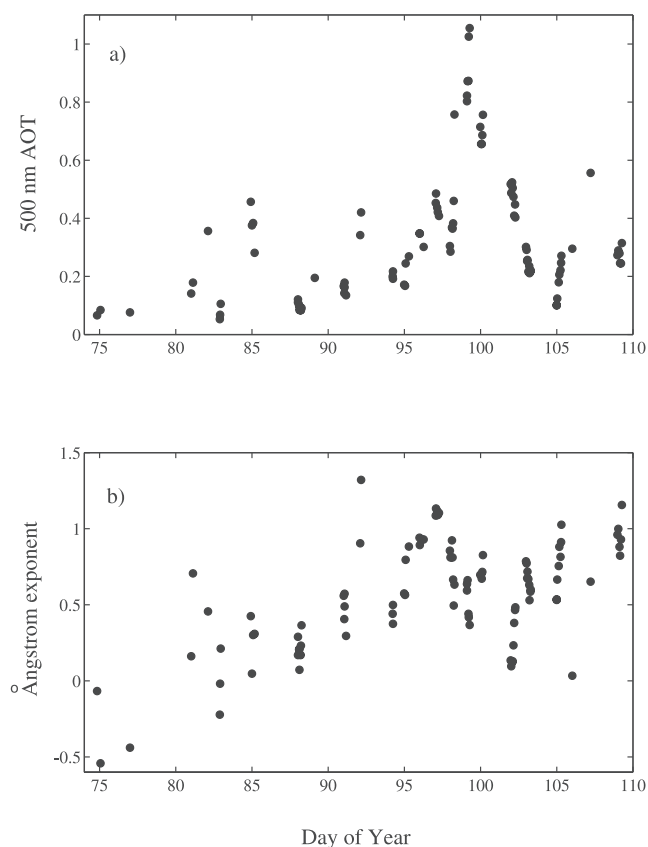


**Figure 2.** Temporal variation of (a) aerosol optical thickness (AOT) at 500 nm and (b) Ångström exponent.

and limitations. The next section shows that the predictions of our model, based on the OPAC database and measured chemistry, agree with some of the inherent and derived optical properties that are observed independently of the OPAC model.

#### 4. Aerosol Optical Thickness and Single-Scattering Albedo

[22] The aerosol optical thickness (AOT) and single-scattering albedo are important parameters for determining the aerosol forcing at the surface, in the atmosphere, and at the top of atmosphere over the low-albedo surface of the ocean. Figure 2a shows the variation in AOT at 500 nm during the cruise (March and April of 2001). The AOT ranges from 0.05 to 1 and has significant daily variability. The lower value of AOT, observed during the first part of cruise, is associated with clear marine air masses of the central Pacific Ocean.

[23] Only during YD85, after the frontal passage, did we measure large AOT in the marine air mass, with values reaching about 0.45 in the morning and 0.3 later that afternoon. Independently, we also observed a large aerosol infrared forcing ( $4.5 \pm 0.7 \text{ W m}^{-2}$ ) using a Fourier Transform interferometer [Vogelmann *et al.*, 2003] that we report here only to stress that the YD85 large optical depth was indeed present. Sea-salt and non-sea-salt sulfates were important components of the aerosol during that day, as seen from the chemical composition analysis (P. K. Quinn *et*

*al.*, Aerosol optical properties measured on board the *Ronald H. Brown* during ACE Asia as a function of aerosol chemical composition and source region, submitted to *Journal of Geophysical Research*, 2003) (hereinafter referred to as Quinn *et al.*, submitted manuscript, 2003) but their values at the surface were not large enough to support such a high AOT. A numerical simulation based on the GOCART model (Mian Chin, private communication) indicates that there was dust at the top of the boundary layer for that day and approximately half of the AOT is attributed to dust. This is interesting, but not unexpected, to see dust transported so far from Asia. Thus we interpret an increase of the AOT above the background (by about 0.2–0.3) as being associated with dust at the top of the boundary layer. The largest AOT (close to 1) was measured in the Sea of Japan during YD99 and was associated with a high relative humidity of about 95% at the surface (Figure 3a). However, the middle atmosphere was dry and the total columnar water vapor was only about  $1.4\text{g/cm}^{-2}$ . During that day the visibility at the surface was poor, which made it difficult to screen for thin clouds covering the Sun.

[24] The Ångström exponent ( $\alpha$  in  $\tau = \beta\lambda^{-\alpha}$ , evaluated for wavelengths between 500–1020 nm) is shown in Figure 2b for the ACE-Asia cruise. Large  $\alpha$  are associated with small particles. The negative values over the central Pacific Ocean correspond to clean marine air masses with a small fraction of submicron particles. Between YD97 and YD103, a mineral dust aloft had significant influence on the optical properties of aerosol as seen by the small Ångström

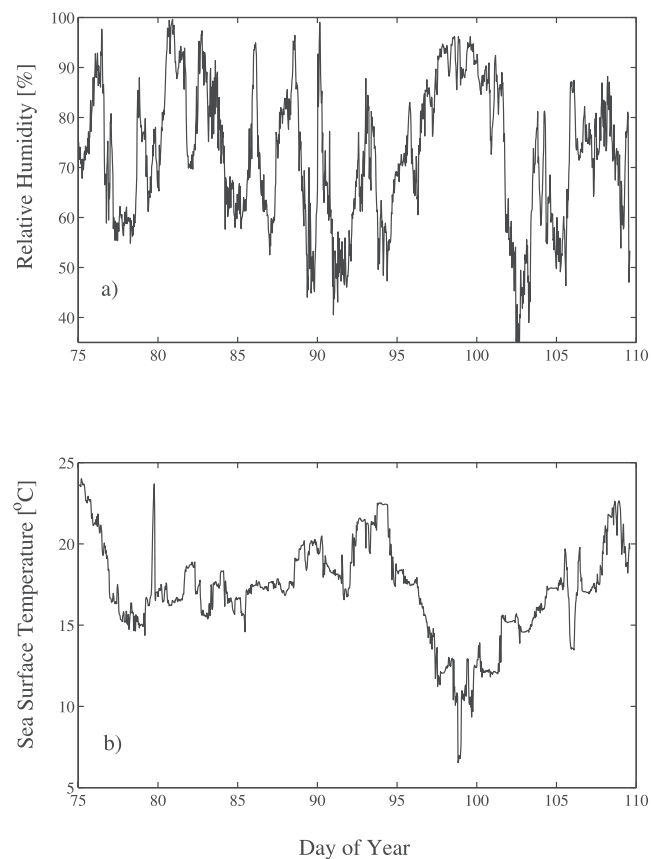


**Figure 3.** (a) Surface relative humidity and (b) sea surface temperature during the ACE-Asia cruise.

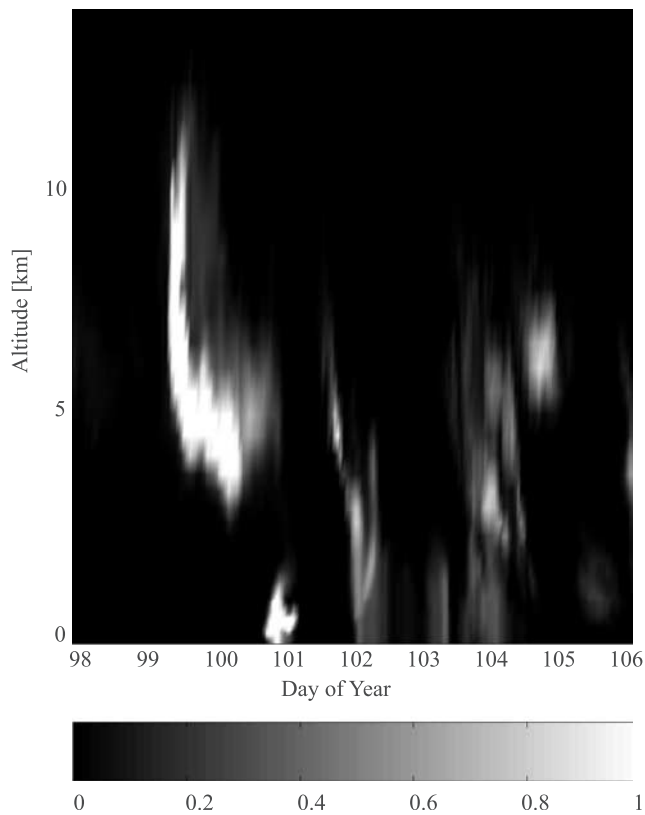


**Figure 4.** Extinction coefficient in arbitrary units obtained from U.S. Navy's (COAMPS) transport model. The model results were interpolated to NOAA ship *R.H. Brown* position.

exponent. However, this is not directly observed in the surface chemistry until YD101 because the dust gradually descended toward the surface. The upper layer dust event between YD99 and YD101 is seen on the U.S. Navy's (COAMPS) transport model (Figure 4). The dust layer spread from 4 to 13 km with the maximum of extinction coefficient about 5 km. YD102 was dominated by dust in boundary layer; in the morning the mass fraction of dust for particles less than  $10\ \mu\text{m}$  in diameter was about 85% and in the afternoon about 55%. The decreasing in dust concentrations at the surface correlated with decreased AOT and increased the Ångström exponent (Figures 2a and 2b).

[25] Figure 5 shows the single-scattering albedo (SSA) obtained by three independent methods. The solid line represents the SSA for ambient RH, based on the total scattering determined by the humidograph nephelometer method, and absorption determined by the PSAP instrument. Note that the absorption coefficient was measured at RH 55% and the SSA for ambient RH was calculated assuming that RH has a negligible influence on the absorption coefficient. The solid circles are the PMEL nephelometer and PSAP-based SSA at 55% relative humidity, and the squares are the SSA calculated with our aerosol-chemical model at ambient RH. During the first part of the cruise, the SSA was conservative (close to 1) because the aerosol was dominated by nonabsorbing sea salt and sulfates. SSA decreased from 0.98 to 0.87 on YD90 due to an increase in absorption, decrease in scattering, and low ambient RH. The low RH was associated with the passage of the cold

front and a cooler and drier air mass (relative humidity decreased to 50% and temperature decreased by  $10^\circ\text{C}$ ). During that event, the decrease in RH (Figure 3a) correlated with an almost four-fold decrease in the sea-salt mass concentration, which dominated the decrease in soot concentration and yielded lower SSA.

[26] Another example, showing the correlation between the SSA and RH, can be seen between YD96 and YD99. The SSA observed at ambient conditions (solid line) and calculated from the model (squares) increased due to increasing relative humidity, but the SSA observed at a constant relative humidity of 55% decreased. This leads to a large SSA difference of 0.06 on YD99 between the constant and ambient RH observations. This large increase of relative humidity was measured only in the first several hundred meters above the sea surface, and was associated with decreasing sea surface temperature (Figure 3b) as we were sailing north (Figure 1).

[27] For days YD100 to YD102, all three methods show good agreement despite the large range of relative humidity values. The Navy transport model Figure 4 indicates for YD100–YD101 dust aloft, which descended and increased concentrations at the surface, and YD102 was governed by a transition to low humidity with dust at the surface. This indicates a smaller effect of humidity on SSA for dust-influenced aerosols when the presence of dust is accompanied by relatively dry air.

[28] Figure 6 shows the SSA as function of relative humidity based on the humidograph measurements of scattering at ambient RH and PSAP measurements of absorption at constant RH = 55% for the section of cruise in the Sea of Japan. Squares on Figure 6 show SSA as a function of the RH for particles with diameters  $D \leq 10\ \mu\text{m}$ .

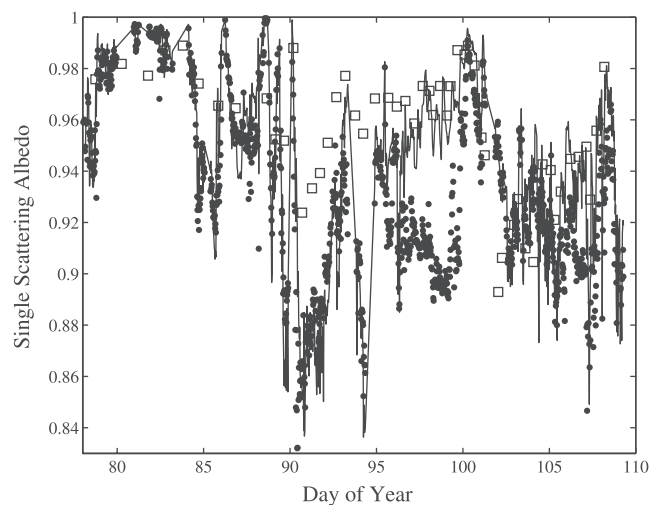


**Figure 5.** Single-scattering albedo (SSA) obtained from three independent methods: The solid line represents the SSA for ambient RH, based on the total scattering determined by the humidograph nephelometer method and absorption determined by the PSAP instrument (the PSAP absorption data were not corrected for changes in RH = 55%); solid circles are the PMEL nephelometer and PSAP-based SSA at 55% relative humidity; and squares give the SSA calculated from our aerosol-chemical model at ambient RH.

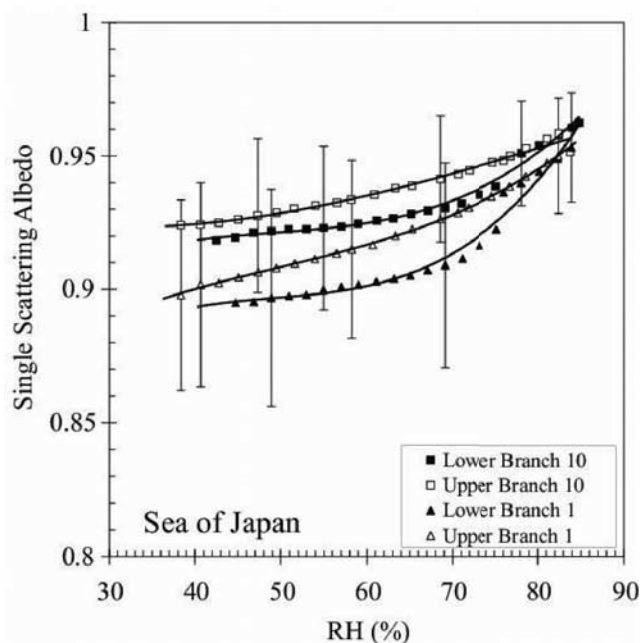


**Figure 6.** The single-scattering albedo from the humidograph as a function of relative humidity in the Sea of Japan (open symbols). The squares correspond to particles with diameter  $D \leq 10 \mu\text{m}$ , and triangles correspond to submicron particles ( $D \leq 1 \mu\text{m}$ ). Open symbols mark the single-scattering albedo measured by humidograph during “up,” and solid symbols mark “down” relative humidity changes.

Triangles show the same relationship but only for particles with diameters  $D \leq 1 \mu\text{m}$ . There is a significant correlation between the SSA and relative humidity ( $r^2 = 0.69$ ) and the observations clearly show an increase of SSA with relative humidity. This effect is important for the aerosol forcing efficiency, which will be discussed later. Influence of the RH on the SSA is larger for smaller particles, because a significant part of the supermicron particles are nonhygroscopic dust.

[29] Because the aerosol light scattering was measured as a function of relative humidity [Carrico *et al.*, 1998], we can plot single-scattering albedo with increasing RH beginning with a “dry” aerosol, and with decreasing RH beginning with a hydrated aerosol [Carrico *et al.*, 2000]. This is on Figure 6, where single-scattering albedo is plotted for almost simultaneous times (separated by approximately 1/2 hour) but for “up” (open symbols) and “down” (solid symbols) relative humidity changes, while assuming that absorption does not change with RH. For small RH the SSA, and consequently aerosol forcing efficiency, depends not only on its absolute value but also on its time change, which may be governed by the air mass transformation. Such transformations may be related to large scale subsidence, frontal passages, or advection over colder surface. However, in what follows, we do not differentiate between the “up” and “down” RH changes because we are focusing on the first-order effects of the relative humidity changes.

[30] The mean value of SSA over the Sea of Japan is 0.95 at ambient condition and 0.92 at 55 % of RH. These values are consistent with SSA derived from recent global

model estimates [Takemura *et al.*, 2002], and are larger (less absorbing) than what has been observed over the Arabian Sea (SSA = 0.89) [Ramanathan *et al.*, 2001] and the Mediterranean Sea (SSA = 0.87) [Markowicz *et al.*, 2002].

## 5. Aerosol Forcing

[31] Of the 15 cruise days in the proximity to Japan, six days had less than 10% cloud cover. We used these days to estimate the aerosol forcing directly from observations. Also, we performed model calculations to show the sensitivity of aerosol forcing to relative humidity and other parameters. In this approach [Satheesh and Ramanathan, 2000], the aerosol radiative forcing at the TOA and at the surface are obtained from radiometric observations. The difference between the TOA and the surface forcing yields the atmospheric forcing (due mostly to the aerosol absorption of solar radiation). The forcing is defined as the effect of aerosol on the net (down minus up) solar flux. We use a hybrid technique [Satheesh and Ramanathan, 2000], in which a model is used to determine the clear-sky radiative fluxes only.

### 5.1. Direct Estimate of Surface and Top of the Atmosphere Aerosol Forcing

[32] The mean daily clear-sky net fluxes at the surface were obtained from a 24-hr average of the downward fluxes measured by Kipp and Zonen pyranometer, subtracting the upward flux calculated using an ocean albedo model. The ocean model included contributions from Fresnel reflection and small background reflection due to phytoplankton contribution. The diurnally averaged net flux at the surface and TOA without aerosol was calculated by the radiative transfer model. In this study we used Modtran version 4.1 [Berk *et al.*, 1998], which is based on the DISORT code [Stamnes *et al.*, 1988]. The model input for these clear-sky calculations are the vertical profiles of temperature and water vapor concentration, which are obtained from the nearest sounding.

[33] Figure 7a shows the daily mean aerosol forcing at the surface as a function of the AOT at 500 nm. Circles represent the aerosol forcing based on observations, and the solid line is a linear fit to these points. Notice that aerosol forcing does not asymptote to zero for zero optical depth (as it should) due to offset errors in the observations and in the modeling. However the slope, obtained from the linear fit of the forcing, is independent of this bias and is used here; this slope is termed the aerosol forcing efficiency (aerosol forcing per unit of AOT). This estimate of the efficiency provides the average radiative effect of regional aerosols. Between YD97 and YD105, the regional aerosol varied between polluted (composed primarily of sulfate, OC, and EC) and pollution mixed with dust (composed primarily of sulfate, OC, EC, and dust) (Quinn *et al.*, submitted manuscript, 2003). Hence the SSA varied between 0.92 and 0.98 due to RH effects and differences in the uptake of water by the dominant chemical components.

[34] The mean daily aerosol forcing efficiency between YD97 and YD105 is  $-59.9 \pm 7.3 \text{ W m}^{-2}$ . In comparison, the mean aerosol forcing efficiency during MINOS is  $-85 \text{ W m}^{-2}$  [Markowicz *et al.*, 2002] and during INDOEX

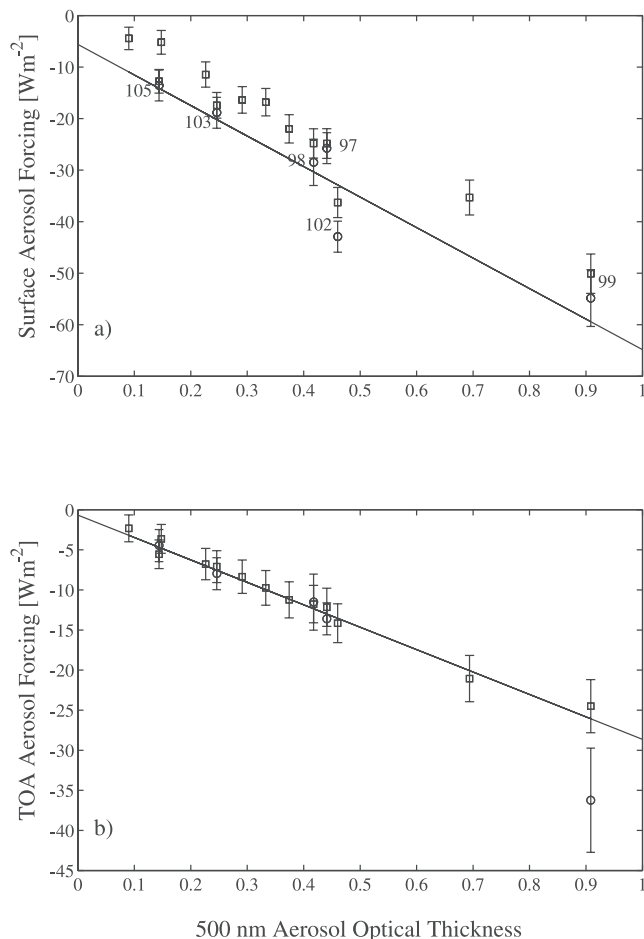


**Figure 7.** (a) The solar aerosol forcing at the Earth's surface (broadband and diurnal averaged) as a function of aerosol optical thickness (AOT); (b) the solar aerosol forcing at the TOA (broadband and diurnal averaged). The open circles in both cases represent the aerosol forcing obtained from observations, squares represent the aerosol forcing obtained from radiative transfer model, and the solid line is a linear fit to the observations.

it is  $-75 \text{ W m}^{-2}$  [Satheesh and Ramanathan, 2000]. The variation in single-scattering albedo, as well as particle sizes may play significant roles in these differences. During the ACE-Asia measurement period, the aerosol over the Sea of Japan was more conservative (SSA closer to 1) compared to these other two campaigns, which leads to a smaller aerosol forcing efficiency at the surface.

[35] The aerosol forcing efficiency (Figure 7a) for YD102 is substantially larger than that found for the other days. This behavior is consistent with a lower value of SSA (in comparison to other days, see Figure 5) that occurs during the dust event with lower RH. This decrease of SSA during the YD102 leads to a  $-10$  to  $-15 \text{ W m}^{-2}$  enhancement in surface forcing. Such change is consistent with a forcing efficiency in the range of  $-80$  to  $-93 \text{ W m}^{-2}$ , rather than  $-60 \text{ W m}^{-2}$ .

[36] The aerosol forcing at the TOA as a function of AOT is shown on Figure 7b. The open squares represent the aerosol forcing determined from CERES observations

(TERRA satellite). We collocated the satellite observing footprint and ship position (maximum deviation of 25 km) when the viewing angle was less than  $60^\circ$ . The instantaneous fluxes were converted to diurnal mean values using the aerosol optical model and Modtran radiative transfer model. The conversion factor varied from 1.9 to 2.0 depending on ship's position and length of day. YD99 was classified by the satellite algorithm as cloudy, probably because of the hazy conditions with a large AOT close to 1. Therefore we did not include this (misclassified) point when deriving the slope. The TOA aerosol forcing efficiency is  $-27.5 \pm 3.9 \text{ W m}^{-2}$ . This result is comparable to the  $-25 \text{ W m}^{-2}$  TOA aerosol forcing efficiency observed during the INDOEX [Satheesh and Ramanathan, 2000].

## 5.2. Modeled Surface and TOA Aerosol Forcing

[37] Up to now, the model results were used to determine the clear-sky flux without aerosols. We aim to investigate the dependence of forcing on changes in relative humidity in more detail. Because our observational data set is limited, we use calculations of the aerosol forcing based on our radiative transfer model. The model inputs for these calculations are the vertical profiles of temperature and water vapor concentration, and the vertical distribution of the aerosol optical properties obtained from the model described in section 3. The aerosol model provides the spectrally dependent, vertical distribution of the aerosol extinction coefficient, the absorption coefficient, and the asymmetry parameter.

[38] A comparison of the downward flux for YD103 (Figure 8a) at the surface between measured (solid line) and modeled flux (solid circles) shows excellent agreement. The model agreement is better quantified on Figure 8b where the data for all days are presented. The model total flux underestimates the observations by  $4.4 \text{ W m}^{-2}$ , and the small deviation (rms  $12.9 \text{ W m}^{-2}$ ) is within the range of pyranometer uncertainty. This good agreement is somewhat surprising given that we assumed constant aerosol composition with height. For example, YD99 is where the transport model indicates an elevated dust layer aloft between 4 and 13 km (Figure 4). A plausible explanation for this agreement is that the optical properties, at the surface and aloft, were not radically different.

[39] The squares in Figure 7a represent the aerosol forcing at the surface obtained from the model, with the slope (aerosol forcing efficiency) of  $-57.0 \pm 3.9 \text{ W m}^{-2}$ . This agrees with the observations for which forcing efficiency is  $-59.9 \pm 7.3 \text{ W m}^{-2}$ . Similarly, the aerosol forcing at the TOA as function of AOT is shown in Figure 7b. Again, the agreement between the model (open squares) and measurements (open circles) is excellent. The TOA aerosol forcing efficiency derived from model is  $-28.0 \pm 3.1 \text{ W m}^{-2}$ , compared to the observed  $-27.5 \pm 3.9 \text{ W m}^{-2}$ .

[40] Figure 9a shows the aerosol forcing as a function of year day (YD). The modeled aerosol forcing is given by open squares and open circles indicate the observations. Values for the observational aerosol forcing were determined by the mean aerosol forcing efficiency (by averaging all data) multiplied by the daily averaged AOT. The background aerosol forcing observed during the Pacific transect was smaller than  $-10 \text{ W m}^{-2}$ , with the exception of YD85

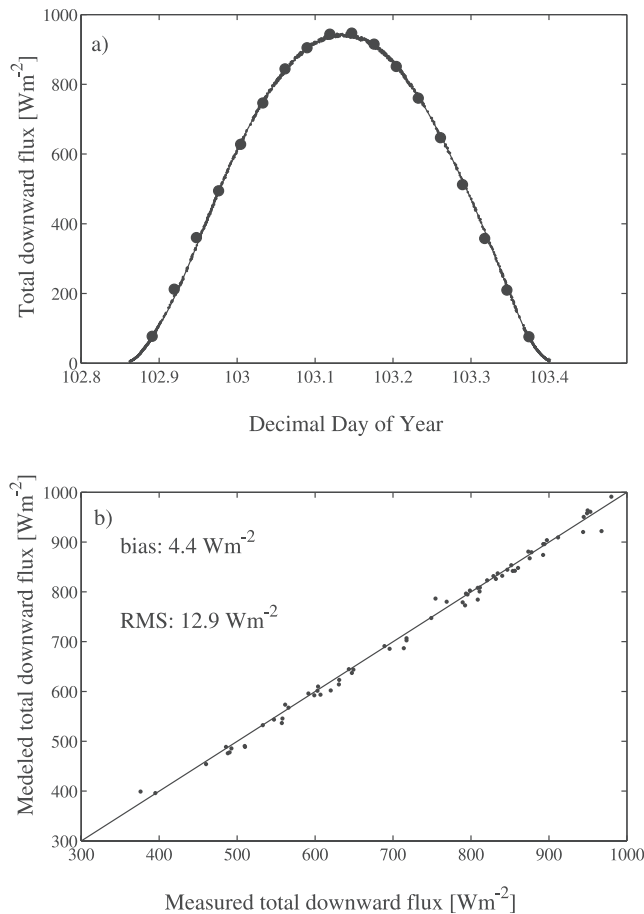


**Figure 8.** (a) YD103 daily cycle of total broadband fluxes at the surfaces. The solid line represents the pyranometer observations, and the solid circles are from the radiative transfer model. (b) Comparison of the measured and estimated surface broadband total fluxes. The solid line corresponds to perfect agreement.

when the forcing increased to  $-22 \text{ W m}^{-2}$ , presumably, due to the sea salt generated by strong winds. The Pacific transect section in Figure 9a requires further explanation. Within that three week period, we observed extratropical cyclones passing by every three to four days with associated cloud systems. Not surprisingly, we were able to measure the optical depth somewhat sporadically during that time. It was hypothesized before [e.g., Jacobson, 2001; Winter and Chylek, 1997] that strengthening of storm tracks may lead to increased sea-salt radiative forcing. Indeed, the YD85 measurements show strong sea-salt radiative forcing dependence on wind speed, but more work remains to be done in this respect.

[41] The TOA aerosol forcing is shown in Figure 9b. The Pacific transect values are small. The Sea of Japan exhibits gradually increasing values with a maximum of  $-24.5 \text{ W m}^{-2}$  for YD99 and YD100, which are caused by relatively conservative scattering. The average value for the cruise is  $-10.6 \text{ W m}^{-2}$ .

[42] The aerosol atmospheric forcing is shown in Figure 9c. The Pacific transect was characterized by a small forcing ( $2$  to  $3 \text{ W m}^{-2}$ ) with the exception of YD85 already discussed. In the Sea of Japan, atmospheric forcing

increased on average to  $10$  to  $15 \text{ W m}^{-2}$ . However, during two days it reached larger values of  $25 \text{ W m}^{-2}$  (YD99) and  $22 \text{ W m}^{-2}$  (YD102), which were associated with the aerosol absorption (see Figure 5) and large optical thickness.

## 6. Relative Humidity Influence on Aerosol Forcing Efficiency

[43] Figure 10 shows the monthly averaged surface relative humidity (NCEP reanalysis) for April 2001. There is a significant gradient of relative humidity caused by the sea surface temperature gradient in the Sea of Japan. In April 2001 the oceanic polar front was positioned at  $38$ – $40^\circ\text{N}$  and the ship was in that region on YD98 and YD99 where the SST gradient was close to  $6.5\text{C}$  (Figure 3b). The warmer air mass-flow from Asia leads to increased RH in the shallow layer close to the surface. For example, on YD99 the relative humidity was  $95\%$  (Figure 3a) but dry, subsidence driven conditions existed above  $500 \text{ m}$ . This resulted in shallow and extended haze conditions in the lower boundary layer for which the AOT was above one and the SSA was  $0.98$ . The increase in relative humidity leads to particle growth, increase in scattering, and the associated increases in AOT, SSA and asymmetry parameter. The AOT increase causes an increase of aerosol forcing at the surface as well as at the TOA. The SSA

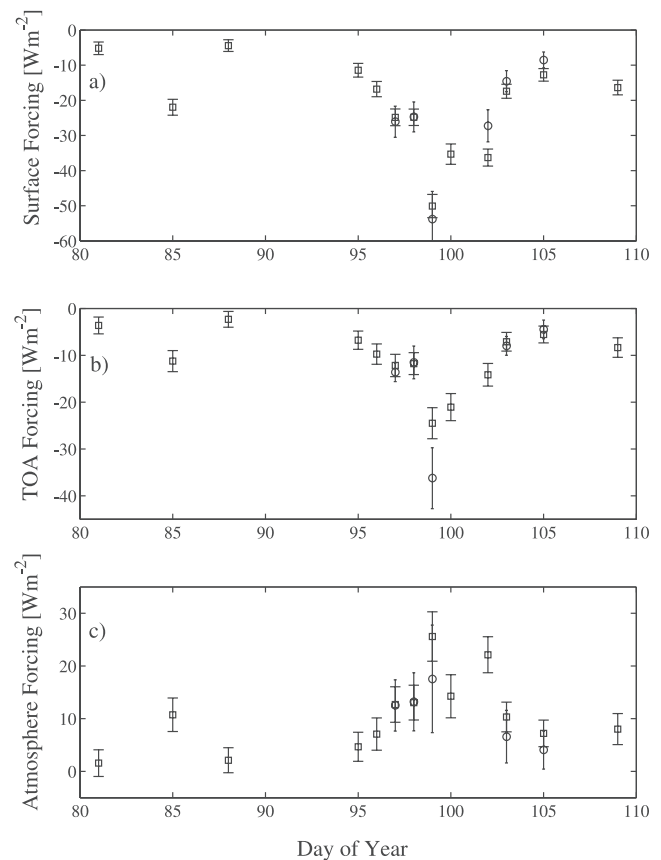


**Figure 9.** (a) Temporal variation of aerosol forcing at the (a) surface, (b) TOA, and (c) atmosphere. The circles correspond to observations and squares represent model results.

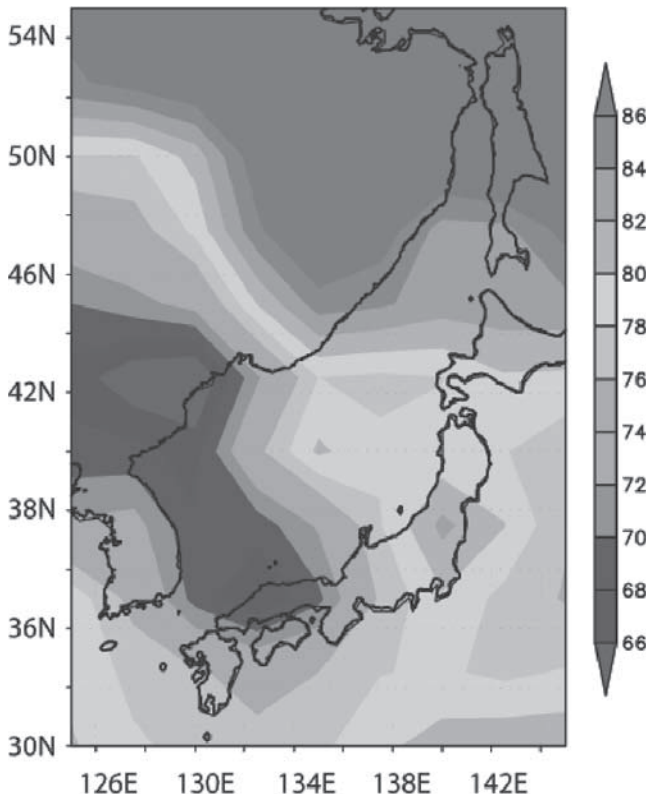


**Figure 10.** Mean monthly surface relative humidity over the Sea of Japan in April 2001.

increase causes aerosol forcing decreases at the surface and an increase at the TOA. The asymmetry parameter increase causes a forcing decrease at the surface as well as at the top of the atmosphere. These are opposite trends and we performed a numerical sensitivity study to determine the net effect on the forcing efficiency (which is, to first approximation, independent of the optical depth).

[44] We modified the optical properties of a shallow, but humid lower layer by assuming a constant 55% relative humidity. Between YD95 and YD99 when the humidity effects were large, radiative transfer calculations show that the aerosol forcing efficiency was enhanced by  $-5$  to  $-10 \text{ W m}^{-2}$  (Figure 11a) at the surface and decreased up to  $2 \text{ W m}^{-2}$  (Figure 11b) at the TOA. In other words, large values of relative humidity caused a decrease in the aerosol forcing efficiency over the Sea of Japan, despite of the significant transport from anthropogenic sources in Asia (including soot).

[45] Figures 12a and 12b show the surface and TOA aerosol forcing efficiency as a function of relative humidity for modeled YD99, which assumes constant relative humidity in the boundary layer up to 2 km. Only the optical properties of the aerosol were modified by RH changes. In this case the change in the surface aerosol forcing efficiency is about  $20 \text{ W m}^{-2}$  between  $\text{RH} = 55\%$  and  $\text{RH} = 95\%$ . This is significantly larger than that presented in Figure 11a because in that case we modified the relative humidity in only the lower boundary layer (approximately 200–300 m). The change of the TOA aerosol forcing efficiency due to relative humidity changes is about  $2.5 \text{ W m}^{-2}$ . These

changes depend on the aerosol growth factors and thus have a similar functional dependence.

### 7. Summary

[46] The transect from Honolulu to Japan aboard the NOAA ship *Ronald H. Brown* during ACE-Asia provided the opportunity for detailed measurements of aerosol properties and their radiative effects. Conditions ranged from “clean” regions of the central Pacific, to highly polluted and dusty conditions in the proximity of Asia and Japan. The large gradient in optical depth observed while passing from the open Pacific Ocean to near the Asian continent is similar to observations during INDOEX [Ramanathan et al., 2001], where the transition between the clean Southern Hemisphere to the polluted Northern Hemisphere was observed.

[47] Close to Asia, we crossed the oceanic polar front at  $38^\circ\text{N}$  in the Sea of Japan, which determined sea surface temperature and relative humidity. We observed hazy conditions when the water was cool and the relative humidity approached 95%. We analyzed the global forecast model results and observed that such behavior is also seen in monthly means. In retrospect, other recent field campaigns devoted to aerosol radiative effects (e.g., MINOS and INDOEX) were conducted in the regions with large relative humidity gradients and reported widespread haze. We show from the direct observations that water uptake changes

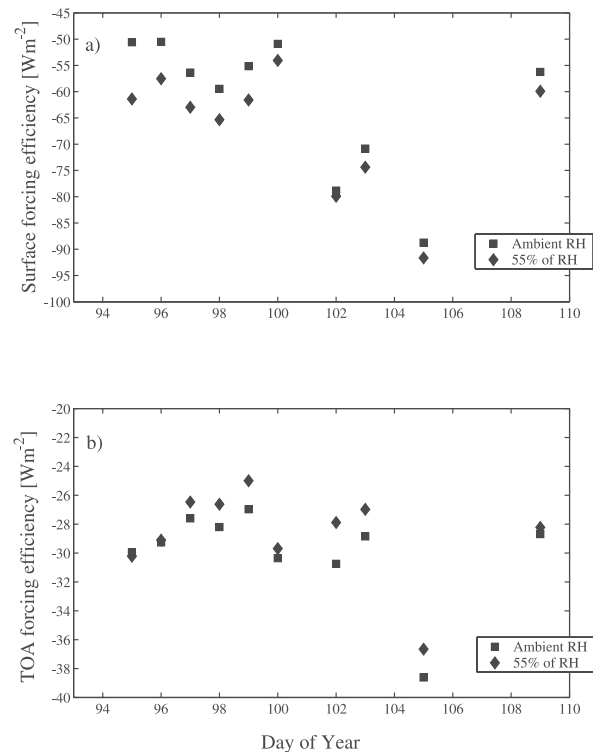


**Figure 11.** Aerosol forcing efficiency as a function of day of year determined from the radiative transfer model. The squares mark aerosol forcing efficiency obtained at ambient relative humidity, and the diamonds corresponds to calculations with maximum 55% of relative humidity in first 1 km of atmosphere.

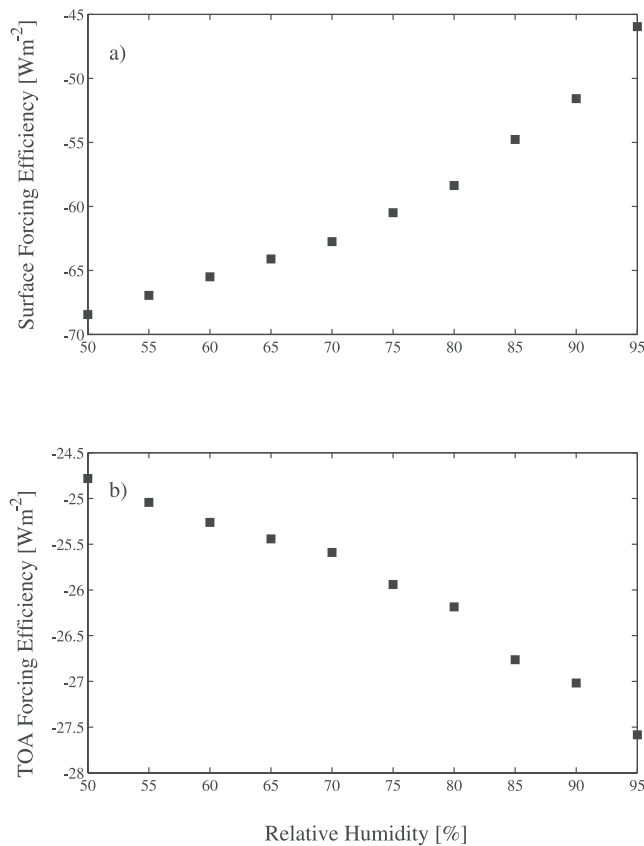


**Figure 12.** Diurnal averaged (a) surface and (b) TOA aerosol forcing efficiencies determined from the radiative transfer model as a function of relative humidity for YD99.

radiative aerosol efficiency. We estimate this aerosol efficiency to be approximately  $-60 \text{ W m}^{-2}$  on the basis of all the data from our cruise in the Sea of Japan. We also provide numerical evidence that a 25% decrease in relative humidity enhances the surface forcing efficiency by 6 to  $10 \text{ W m}^{-2}$ . We did not model RH influence on forcing itself but recent studies show that the role of hygroscopic growth on direct radiative forcing at the surface is significant [Im *et al.*, 2001; Kotchenruther *et al.*, 1999]. A recent study suggests that aerosol efficiency is largely invariant in space and time, and is approximately equal to  $-80 \text{ W m}^{-2}$  [Kaufman *et al.*, 2002]. However, our results point out that there may be important synoptic scale regional differences caused by relative humidity variations.

[48] **Acknowledgments.** KMM was supported by a Fulbright grant. PJF was supported by the National Science Foundation Climate Dynamics program and by the ONR Program Element PE0602435N. A. M. Vogelmann was supported by NSF (ATM-0109135).

## References

Anderson, T. L., and J. A. Ogren, Determining aerosol radiative properties using the TSI 3563 integrating nephelometer, *Aerosol Sci Tech*, 29, 57–69, 1998.

Bates, T. S., B. J. Huebert, J. L. Gras, F. B. Griffiths, and P. A. Durkee, International Global Atmospheric Chemistry (IGAC) project's first aerosol characterization experiment (ACE 1): Overview, *J. Geophys. Res.*, 103, 16,297–16,318, 1998.

Berk, A., L. S. Bernstein, G. P. Anderson, P. K. Acharya, D. C. Robertson, J. H. Chetwynd, and S. M. Adler-Golden, MODTRAN cloud and

multiple scattering upgrades with application to AVIRIS, *Remote Sens. Environ.*, 65, 367–375, 1998.

Bond, T. C., T. L. Anderson, and D. Campbell, Calibration and intercomparison of filter-based measurements of visible light absorption by aerosols, *Aerosol Sci. Technol.*, 30, 582–600, 1999.

Carrico, C. M., M. J. Rood, and J. A. Ogren, Aerosol light scattering properties at Cape Grim, Tasmania, during the First Aerosol Characterization Experiment (ACE 1), *J. Geophys. Res.*, 103, 16,565–16,574, 1998.

Carrico, C. M., M. J. Rood, J. A. Ogren, C. Neususs, A. Wiedensohler, and J. Heintzenberg, Aerosol optical properties at Sagres, Portugal during ACE-2, *Tellus, Ser. B*, 52, 694–715, 2000.

Chin, M., P. Ginoux, S. Kinne, O. Torres, B. N. Holben, B. N. Duncan, R. V. Martin, J. A. Logan, A. Higurashi, and T. Nakajima, Tropospheric aerosol optical thickness from the GOCART model and comparisons with satellite and Sun photometer measurements, *J. Atmos. Sci.*, 59, 461–483, 2002.

Collins, W. D., P. J. Rasch, B. E. Eaton, B. V. Khattatov, J. F. Lamarque, and C. S. Zender, Simulating aerosols using a chemical transport model with assimilation of satellite aerosol retrievals: Methodology for INDOEX, *J. Geophys. Res.*, 106, 7313–7336, 2001.

Flatau, P. J., K. A. Fuller, and D. W. Mackowski, Scattering by 2 spheres in contact—Comparisons between discrete-dipole approximation and modal analysis, *Appl. Opt.*, 32, 3302–3305, 1993.

Hanel, G., and B. Zankl, Aerosol size and relative humidity: Water uptake by mixture of salts, *Tellus*, 31, 478–486, 1979.

Hess, M., P. Koepke, and I. Schult, Optical properties of aerosols and clouds: The software package OPAC, *Bull. Am. Meteorol. Soc.*, 79, 831–844, 1998.

Hobbs, P. V., An overview of the University of Washington airborne measurements and results from the Tropospheric Aerosol Radiative Forcing Observational Experiment (TARFOX), *J. Geophys. Res.*, 104, 2233–2238, 1999.

Holben, B. N., *et al.*, An emerging ground-based aerosol climatology: Aerosol optical depth from AERONET, *J. Geophys. Res.*, 106, 12,067–12,097, 2001.

Im, J. S., V. K. Saxena, and B. N. Wenny, An assessment of hygroscopic growth factors for aerosols in the surface boundary layer for computing direct radiative forcing, *J. Geophys. Res.*, 106, 20,213–20,224, 2001.

Intergovernmental Panel on Climate Change, *Climate Change 2001: The Scientific Basis, Contribution of Working Group I to the Third Assessment Report of the Intergovernmental Panel on Climate Change*, edited by J. T. Houghton *et al.*, 881 pp., Cambridge Univ. Press, New York, 2001.

Jacobson, M. Z., Global direct radiative forcing due to multicomponent anthropogenic and natural aerosols, *J. Geophys. Res.*, 106, 1551–1568, 2001.

Kaufman, Y. J., *et al.*, Smoke, Clouds, and Radiation-Brazil (SCAR-B) experiment, *J. Geophys. Res.*, 103, 31,783–31,808, 1998.

Kaufman, Y. J., D. Tanre, B. N. Holben, S. Mattoo, L. A. Remer, T. F. Eck, J. Vaughan, and B. Chatenet, Aerosol radiative impact on spectral solar flux at the surface, derived from principal-plane sky measurements, *J. Atmos. Sci.*, 59, 635–646, 2002.

Kotchenruther, R. A., P. V. Hobbs, and D. A. Hegg, Humidification factors for atmospheric aerosols off the mid-Atlantic coast of the United States, *J. Geophys. Res.*, 104, 2239–2251, 1999.

Lelieveld, J., *et al.*, Global air pollution crossroads over the Mediterranean, *Science*, 298, 794–799, 2002.

Loeb, N. G., and S. Kato, Top-of-atmosphere direct radiative effect of aerosols over the tropical oceans from the Clouds and the Earth's Radiant Energy System (CERES) satellite instrument, *J. Clim.*, 15, 1474–1484, 2002.

Malm, W. C., J. F. Sisler, D. Huffman, R. A. Eldred, and T. A. Cahill, Spatial and seasonal trends in particle concentration and optical extinction in the United States, *J. Geophys. Res.*, 99, 1347–1370, 1994.

Markowicz, K. M., P. J. Flatau, M. V. Ramana, P. J. Crutzen, and V. Ramanathan, Absorbing Mediterranean aerosols lead to a large reduction in the solar radiation at the surface, *Geophys. Res. Lett.*, 29(20), 1968, doi:10.1029/2002GL015767, 2002.

Morys, M., F. M. Mims, S. Hagerup, S. E. Anderson, A. Baker, J. Kia, and T. Walkup, Design, calibration, and performance of MICROTOS II handheld ozone monitor and Sun photometer, *J. Geophys. Res.*, 106, 14,573–14,582, 2001.

Quinn, P. K., D. J. Coffman, T. S. Bates, T. L. Miller, J. E. Johnson, K. Voss, E. J. Welton, and C. Neususs, Dominant aerosol chemical components and their contribution to extinction during the Aerosols99 cruise across the Atlantic, *J. Geophys. Res.*, 106, 20,783–20,809, 2001.

Quinn, P. K., D. J. Coffman, T. S. Bates, T. L. Miller, J. E. Johnson, E. J. Welton, C. Neususs, M. Miller, and P. J. Sheridan, Aerosol optical properties during INDOEX X999: Means, variability, and controlling factors, *J. Geophys. Res.*, 107(D19), 8020, doi:10.1029/2000JD000037, 2002.

- Raes, F., T. Bates, F. McGovern, and M. Van Liedekerke, The 2nd Aerosol Characterization Experiment (ACE-2): General overview and main results, *Tellus, Ser. B*, 52, 111–125, 2000.
- Ramanathan, V., et al., Indian Ocean Experiment: An integrated analysis of the climate forcing and effects of the great Indo-Asian haze, *J. Geophys. Res.*, 106, 28,371–28,398, 2001.
- Satheesh, S. K., and V. Ramanathan, Large differences in tropical aerosol forcing at the top of the atmosphere and Earth's surface, *Nature*, 405, 60–63, 2000.
- Stamnes, K., S. C. Tsay, W. Wiscombe, and K. Jayaweera, Numerically stable algorithm for discrete-ordinate-method radiative transfer in multiple scattering and emitting layered media, *Appl. Opt.*, 27, 2502–2509, 1988.
- Takemura, T., T. Nakajima, O. Dubovik, B. N. Holben, and S. Kinne, Single-scattering albedo and radiative forcing of various aerosol species with a global three-dimensional model, *J. Clim.*, 15, 333–352, 2002.
- Turpin, B. J., and H. J. Lim, Species contributions to PM<sub>2.5</sub> mass concentrations: Revisiting common assumptions for estimating organic mass, *Aerosol Sci. Technol.*, 35, 602–610, 2001.
- Vogelmann, A. M., P. J. Flatau, M. Szczodrak, K. M. Markowicz, and P. J. Minnett, Observations of large aerosol infrared forcing at the surface, *Geophys. Res. Lett.*, 30(12), 1655, doi:10.1029/2002GL016829, 2003.
- Welton, E. J., et al., Ground-based lidar measurements of aerosols during ACE-2: Instrument description, results, and comparisons with other ground-based and airborne measurements, *Tellus, Ser. B*, 52, 636–651, 2000.
- Wielicki, B. A., Clouds and the Earth's Radiant Energy System (CERES)-An Earth Observing System Experiment, *Bull. Am. Meteorol. Soc.*, 77, 1590, 1996.
- Winter, B., and P. Chylek, Contribution of sea salt aerosol to the planetary clear-sky albedo, *Tellus, Ser. B*, 49, 72–79, 1997.
- 
- D. Bates, Physics Department, University of Miami, Coral Gables, FL 33124, USA.
- C. M. Carrico, Department of Atmospheric Science, Colorado State University, Ft. Collins, CO 80523, USA.
- M. K. Flatau, P. J. Flatau, and M. Liu, Naval Research Laboratory, 7 Grace Hopper Avenue, Stop 2, Monterey, CA 93943-5502, USA.
- K. M. Markowicz, Institute of Geophysics, University of Warsaw, Pasteura 7, 02093 Warsaw, Poland. (kmark@igf.fuw.edu.pl)
- P. K. Quinn, Pacific Marine Environmental Laboratory, NOAA, 7600 Sand Point Way NE, Seattle, WA 98115, USA.
- M. J. Rood, Department of Civil and Environmental Engineering, University of Illinois at Urbana-Champaign, Urbana, IL 61801, USA.
- A. M. Vogelmann, Center for Atmospheric Sciences, Scripps Institution of Oceanography, University of California, San Diego, 8602 La Jolla Shores Drive, La Jolla, CA 92037, USA.